ACS OMEGA

Open Access



http://pubs.acs.org/journal/acsodf

Article

# Construction of 2D/3D g-$C_3N_4$/BiOI Photocatalysts with p−n Heterojunction and Their Performance in Photocatalytic Degradation of Amaranth Dye

Junsheng Li, Li Guan, Liming Jiang, Meiyan Xu, Jiahui Li, Jinlong Zuo, Chong Tan, and Zhi Xia*

Cite This: *ACS Omega* 2024, 9, 361−370

Read Online

ACCESS | Metrics & More | Article Recommendations

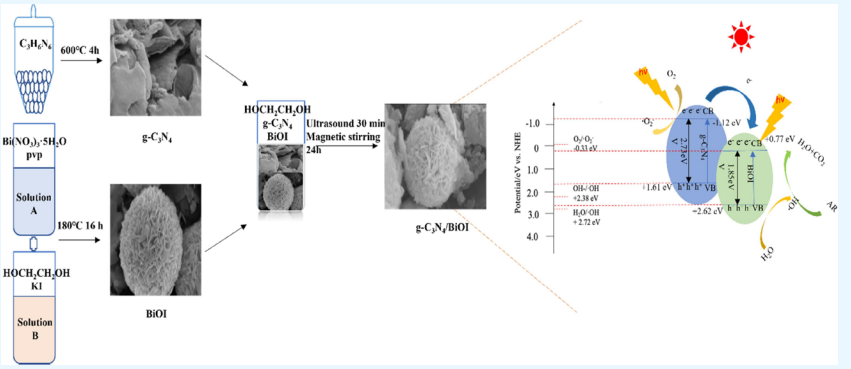


**ABSTRACT:** The g-$C_3N_4$ (graphitic carbon nitride)/BiOI (bismuth oxyiodide) photocatalysts, boasting a unique nanomicrosphere architecture, were synthesized through a tripartite process involving heat polycondensation, hydrothermal treatment, and hybrid methods, using melamine, bismuth nitrate, and potassium iodide as starting materials. The photocatalyst was comprehensively characterized and analyzed while its efficacy in photocatalytic degradation of amaranth (AR) under various lighting conditions was investigated, and the catalytic mechanism was determined by kinetic analysis and free radical scavenging experiments. The results showed that g-$C_3N_4$ formed a strong bond with BiOI. The resulting composite catalyst retains the inherent 2D lamellar structure of g-$C_3N_4$, as well as the 3D microsphere structure of BiOI, thereby creating heterojunctions via p−n interactions. Under visible light exposure, g-$C_3N_4$/BiOI-15% demonstrated optimal catalytic performance, achieving a degradation rate of 74.64% for AR and exhibiting the highest rate constant. Radical tests confirmed that $-O_2^-$ (superoxide anion) plays a crucial role as active species in the photocatalytic reaction.

## 1. INTRODUCTION

Photocatalytic degradation is an eco-friendly, highly efficient, and cost-effective technology for breaking down food dyes in wastewater.[1] Due to its unique structural and chemical properties, $TiO_2$ (titanium dioxide) excels in photocatalytic degradation.[2] However, its application scope remains limited because of its wide band gap, low adsorption capacity, and restriction to ultraviolet light absorption.[3] Consequently, there is an imperative to engineer photocatalysts that are responsive to reactions triggered by visible light. Graphitic carbon nitride (g-$C_3N_4$) has emerged as a focus of research in the field of environmental remediation materials, owing to its advantageous features including a stable layered structure, chemical inertness, solar absorption capacity, and a band gap width of 2.6−2.8 eV—narrower than the 3.2 eV band gap of $TiO_2$.[4] Cui[5] successfully fabricated multilayer porous g-$C_3N_4$ nanosheets through the heat polycondensation of ammonium thiocyanate, demonstrating effective performance in decomposing aquahydrogen under visible-light catalytic conditions. Similarly, Jiang[6] prepared porous sulfur-doped g-$C_3N_4$ nanotubes, which exhibited outstanding efficacy in the degradation of tetracycline.

Regrettably, g-$C_3N_4$ is hampered by a narrow range of visible spectral responsiveness, rapid carrier recombination, and a limited specific surface area, all of which undermine its photocatalytic degradation capabilities. These limitations have restricted its efficacy in practical applications. Therefore, modifications to g-$C_3N_4$ are essential for bolstering its catalytic performance.[7,8] Various approaches—such as morphological adjustments, elemental doping, and semiconductor coupling—

Received: August 2, 2023
Revised: December 9, 2023
Accepted: December 18, 2023
Published: December 28, 2023

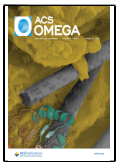

Scheme 1. Diagram of the Synthetic Process of 2D/3D g-$C_3N_4$/BiOI Heterojunction

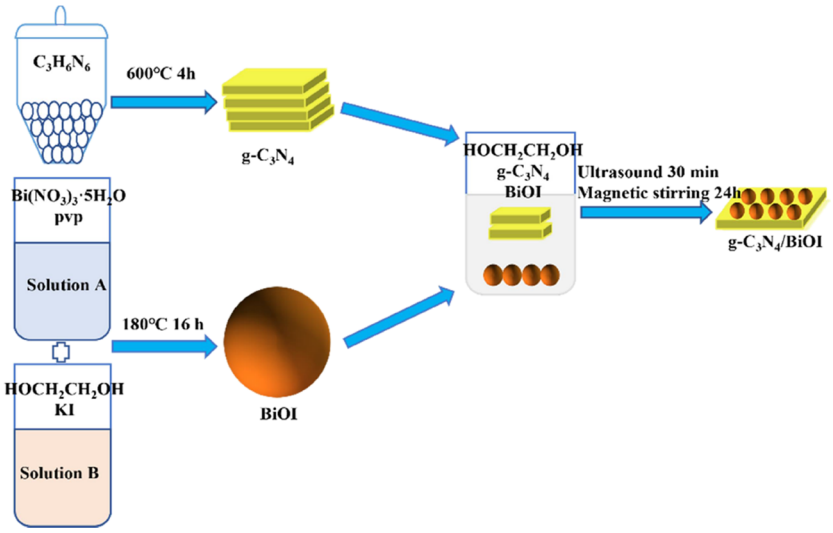


have been employed to mitigate these shortcomings and enhance its catalytic efficacy.[9] Among these, semiconductor coupling stands out as a particularly effective method that involves pairing g-$C_3N_4$ with other semiconductor materials to create heterostructures. Such heterojunctions guide photogenerated electrons and holes in specific directions, thereby mitigating recombination and augmenting charge separation, which in turn improves the material's overall catalytic performance.[10] In a noteworthy example, Liu et al.[11] fabricated a composite catalyst by combining $NiFe_2O_4$ (nickel ferrite) and g-$C_3N_4$. This composite, particularly in its 10%-$NiFe_2O_4$/g-$C_3N_4$ form, achieved an impressive 94.5% degradation rate of tetracycline hydrochloride within 80 min.

Bismuth oxyiodide (BiOI) exhibits excellent photoresponsiveness, photocatalytic activity, and stability primarily due to its layered structure. This unique configuration facilitates effective electron−hole separation and minimizes hole complexation efficiency while also possessing a narrow band gap. However, conventional photocatalysts, including BiOI, often suffer from limitations such as a small specific surface area, inadequate light absorption, and a high rate of electron−hole complexation. To address these shortcomings, BiOI is frequently combined with g-$C_3N_4$ to form heterogeneous structures, thereby enhancing the composite catalyst's performance. Specifically, Li[12] engineered BiOI/g-$C_3N_4$ S-type heterojunction photocatalysts featuring a tightly packed architecture by loading BiOI onto g-$C_3N_4$ substrates. Remarkably, under visible light irradiation, these composite catalysts achieved photodegradation efficiencies nearing 100% for tetracycline hydrochloride and 46% for *p*-chlorophenol, outperforming other photocatalysts in comparative studies. While numerous reports have explored the potential of g-$C_3N_4$/BiOI composites for degrading pollutants, there is a noticeable gap in research concerning their efficacy in breaking down amaranth dye.[13] Therefore, we further investigated the photodegradation performance and underlying mechanisms of this composite catalyst specifically for amaranth dye, aiming to offer valuable insights for its industrial application in food dye degradation.

In this study, composite catalysts of g-$C_3N_4$/BiOI were synthesized through a three-step process involving thermal polycondensation, hydrothermal techniques, and a mixing method. The efficiency and mechanism of the catalysts' pollutant degradation capabilities were rigorously assessed through kinetic analysis and free radical masking experiments, using AR as a model pollutant.

## 2. EXPERIMENTAL SECTION

**2.1. Materials.** Melamine, anhydrous ethanol, bismuth nitrate, potassium iodide, polyvinylpyrrolidone, ethylene glycol, sodium sulfate, and amaranthine analytical purity were acquired from Tianjin Fuyu Fine Chemical Co., Ltd.

**2.2. Fabrication of Photocatalysts.** Preparation of the g-$C_3N_4$ powder: melamine (5 g) was calcined at 600 °C for 4 h. After cooling, grind into powder and wash with deionized water and anhydrous ethanol.

BiOI powder preparation: bismuth nitrate (1.94 g) and polyvinylpyrrolidone (0.1 g) were dispersed into water (38 mL) to obtain solution A. Potassium iodide (0.66 g) was dispersed into ethylene glycol (38 mL) to obtain solution B. A and B were mixed and reacted in a high-pressure reactor at 180 °C for 16 h, cooled to room temperature, rinsed with deionized water and anhydrous ethanol, and dried at 80 °C.

As shown in Scheme 1, taking synthesizing the nanocomposite of g-$C_3N_4$/BiOI with mass ratios of 5:100, 10:100,15:100, 20:100, 25:100, and 30:100 for examples (named as g-$C_3N_4$/BiOI-X%), g-$C_3N_4$ and BiOI were sonicated for 30 min, magnetically stirred for 24 h, and dried at 80 °C.

**2.3. Characterization.** The crystal structure of the product was determined by using a diffractometer (XRD, D8-ADVANCE). The product morphology was observed by scanning electron microscopy (FE-SEM, S-4800) and transmission electron microscopy (TEM, JEM-2100F). X-ray photoelectron spectroscopy (XPS, ESCALAB 250) was used to obtain X-ray photoelectron spectroscopy (XPS, ESCALAB 250), and peak positions were calibrated by C 1s (284.6 eV) to characterize the chemical composition of the product. Fourier transform infrared spectra (FT-IR, VERTEX 80) were obtained to analyze the chemical bonds and functional groups. A UV−vis spectrophotometer (UV-2550) was used to record the UV−vis diffuse reflectance spectra (UV−vis DRS). Photoluminescence spectra (PL) were recorded with a photoluminescence spectrometer (F-7000). Measurement of specific surface area, pore size, and pore size distribution with a specific surface area measuring instrument (Voltas VDSorb-90ii) was performed.


https://doi.org/10.1021/acsomega.3c05569
ACS Omega 2024, 9, 361−370

The zeta potential was measured by using a zeta potential analyzer (Zetasizer Nano-ZS).

**2.4. Photochemical Experiment.** The electrochemical properties of the materials were examined by a photoelectrochemical workstation (CHI 760E) with a platinum electrode as the counter electrode, Ag/AgCl as the reference electrode, a working electrode, and sodium sulfate ($Na_2SO_4$) as the reference solution (0.2 mol/L). The materials and Nafion solution were added to the ethanol solution (95%) and mixed separately and then applied to the working electrode.

**2.5. Photocatalytic Degradation.** The effectiveness of the synthesized g-$C_3N_4$/BiOI photocatalyst was evaluated by measuring the photodegradation of amaranth (AR) under illumination from a 250 W mercury lamp positioned 10 cm away from a specially designed 100 mL quartz reactor. Prior to light exposure, 10 mg of the g-$C_3N_4$/BiOI catalyst was added to 100 mL of a 10 mg/L AR solution and agitated vigorously for 30 min in darkness to achieve adsorption−desorption equilibrium with the environmental pollutants on the photocatalyst's outer surface. Control experiments, conducted without the photocatalyst, helped isolate the effects of light irradiation on AR degradation. Concentration changes in AR were monitored at 522 nm wavelength intervals every 10 min using a UV-2550 spectrophotometer.

## 3. RESULTS AND DISCUSSION

Figure 1 illustrates two unique diffraction peaks for pure g-$C_3N_4$ nanosheets at 13.1 and 27.4°. These peaks correspond to the

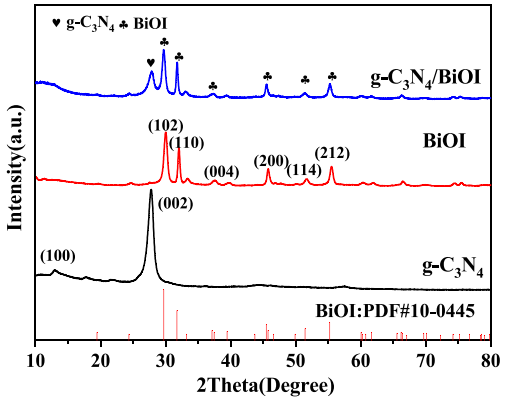


**Figure 1.** XRD patterns of g-$C_3N_4$,BiOI, and g-$C_3N_4$/BiOI.

planar triazine ring structure on the (100) crystallographic plane and the interlayer stacking structure of conjugated aromatic compounds on the (002) plane, respectively, according to the g-$C_3N_4$ standard card (JCPDS 87−1526).[14] Contrasting this with the BiOI standard card (JCPDS 10−0445),[15] BiOI exhibits diffraction peaks at 2$\theta$ angles of 19.3, 24.3, 29.6, 31.6, 39.4, 45.4, 51.3, and 55.1°. These peaks are attributed to the tetragonal BiOI structures on the crystallographic planes (002), (101), (102), (110), (004), (200), (114), and (212), respectively. The composite g-$C_3N_4$/BiOI material displays diffraction patterns closely resembling those of pure g-$C_3N_4$ and BiOI, characterized by sharp and intense peaks. Notably, no extraneous peaks are observed, suggesting effective binding between g-$C_3N_4$ and BiOI. This binding is presumed to facilitate the directional transport of photogenerated electrons on the composite surface, thereby enhancing photocatalytic efficiency.[16] However, the composite does not exhibit the (100) planar peak typical of g-$C_3N_4$. Additionally, there is a noticeable reduction in the intensity of the (002) planar peaks. Possible explanations for these observations include (1) BiOI's covering of the g-$C_3N_4$ surface, which impedes X-ray diffraction; (2) the inherently weaker diffraction signal from g-$C_3N_4$ compared to BiOI[17]; and (3) the comparatively lower amount and crystallinity of g-$C_3N_4$ in the composite, which results in a high degree of dispersion.[18]

The compositions of chemical bonds and functional groups in g-$C_3N_4$/BiOI, BiOI, and g-$C_3N_4$ were examined using FT-IR spectroscopy, especially since their XRD patterns did not reveal the presence of the (100) crystal planes. According to the FT-IR spectra depicted in Figure 2, there are no discernible shifts in

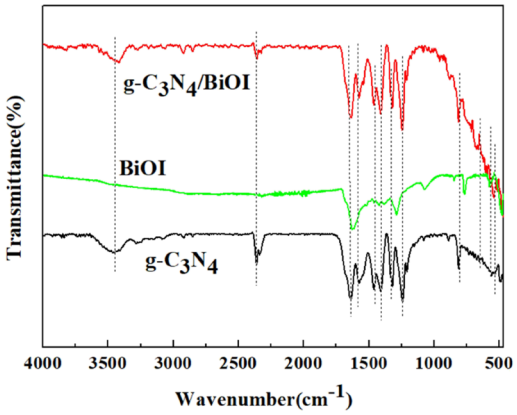


**Figure 2.** FT-IR spectra of various g-$C_3N_4$/BiOI, BiOI, and g-$C_3N_4$ material.

peak positions before and after g-$C_3N_4$'s bonding with BiOI. The observed stretching peaks, ranging between 1700 and 1250 $cm^{-1}$ and at 800 and 890 $cm^{-1}$, can be attributed to the stretching vibrations of the triazine ring skeleton and the triazine moiety in g-$C_3N_4$. Concurrently, Bi−O stretching peaks were identifiable at 665 and 519 $cm^{-1}$.[19] These FT-IR spectral features confirm the successful formation of the g-$C_3N_4$/BiOI composite, as they exhibit characteristic peaks of both g-$C_3N_4$ and BiOI.

The comprehensive spectra of g-$C_3N_4$ and g-$C_3N_4$/BiOI, as shown in Figure 3a, reveal the presence of five key elements: Bi, I, C, N, and O, signifying the successful synthesis of the g-$C_3N_4$/BiOI composites. This finding aligns with XRD and FT-IR analyses, confirming both the coexistence of BiOI and g-$C_3N_4$ within the composite system and the absence of extraneous impurities. Figure 3b illustrates the C 1s XPS spectra, where the C peaks at 284.7 and 288.1 eV in g-$C_3N_4$ are attributed to the $sp^2$ hybridization of C−C and N−C═N bonds.[20,21] Similarly, the C peak at 287.6 eV in g-$C_3N_4$/BiOI corresponds to the $sp^2$ hybridization of g-$C_3N_4$'s N−C═N structure. In Figure 3c, the N 1s peaks at 398.3 and 398.8 eV in both materials are linked to the $sp^2$ hybridized C−N structure, while the peak at 400.2 eV is associated with the tertiary nitrogen group.[19] Figure 3d features O 1s peaks at 530.8 and 532.2 eV, which correlate with low binding energy hydroxyl groups adsorbed onto the BiOI lattice and higher binding energy chemisorbed oxygen in the surface's oxygen-deficient region, respectively. These oxygen and hydroxyl groups on the surface serve as electron and hole traps, enhancing photocatalytic efficiency by forming highly oxidizing hydroxyl radicals.[22] In the context of g-$C_3N_4$/BiOI, Figure 3e identifies two unique peaks at 158.9 and 164.3 eV, representing Bi $4f^{5/2}$ and Bi $4f^{7/2}$ states, respectively, and indicating the presence of $Bi^{3+}$ ions. Figure 3f displays two


https://doi.org/10.1021/acsomega.3c05569
ACS Omega 2024, 9, 361−370

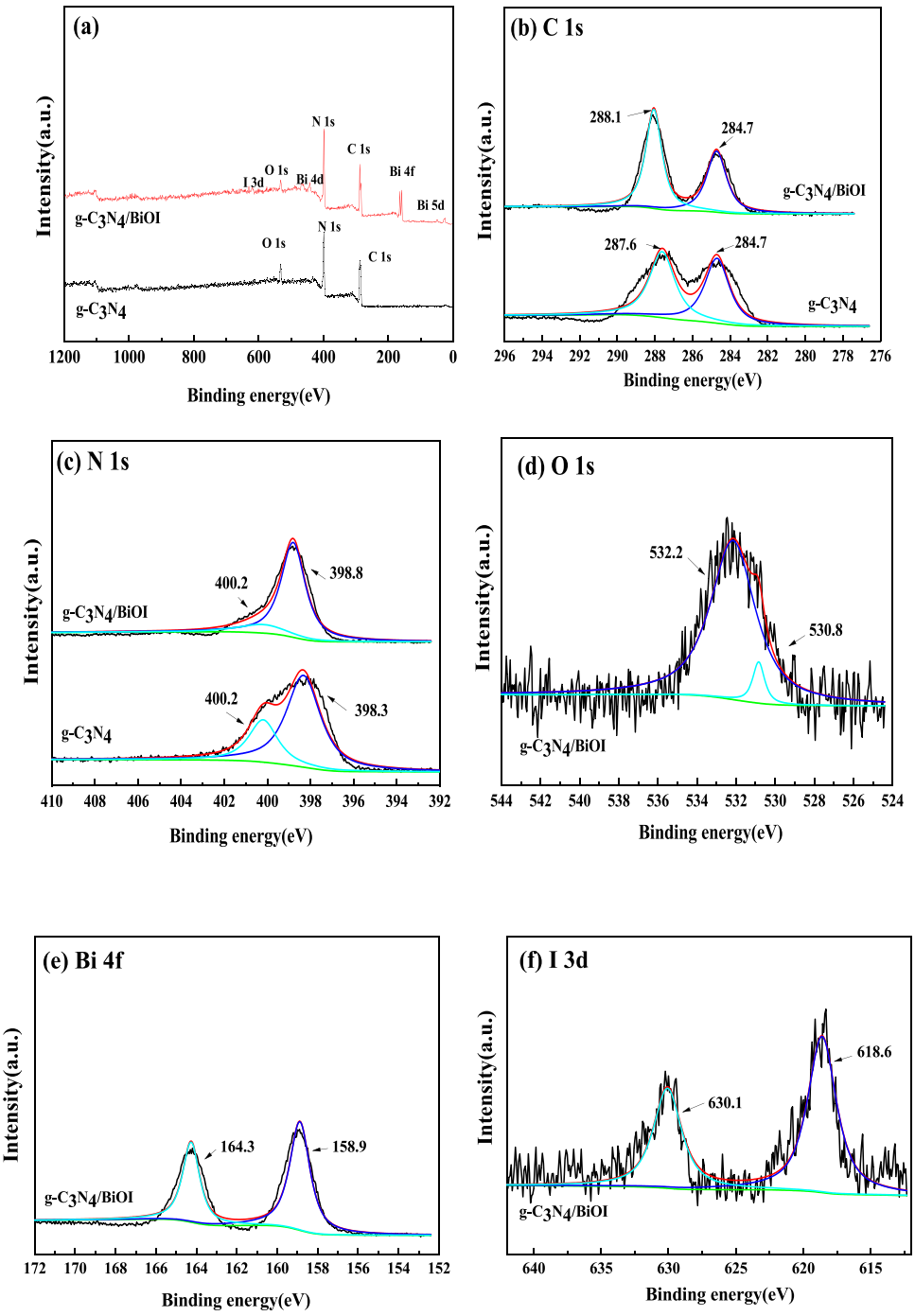


**Figure 3.** High-resolution XPS spectra of g-$C_3N_4$ /BiOI: (a) all spectra, (b) C 1s, (c) N 1s, (d) O 1s, (e) Bi 4f, and (f) I 3d.

distinct peaks at 630.1 and 618.6 eV, confirming the existence of iodine in the form of $I^-$ ions. Notably, the subtle shift in the C and N peaks toward higher binding energies suggests an interaction between g-$C_3N_4$ and BiOI. This interaction leads to g-$C_3N_4$ acquiring additional electrons due to the disparity in atomic sizes between C and N, generating a negative charge. Consequently, $Bi^{3+}$ acts as the active center for N atoms through electrostatic adsorption, facilitating the attachment of BiOI to the surface of g-$C_3N_4$ and resulting in a heterogeneous composite structure.[23]

As illustrated in Figure 4a,b, g-$C_3N_4$ features 2D lamellar structures of varying dimensions that are intricately interwoven and stacked. Some of these structures exist even as monolayers. In Figure 4c,d, g-$C_3N_4$ is shown to form 3D flower-like microspheres, with a diameter of approximately 1.5 $\mu$m, consisting of alternating nanosheets. These structural features are advantageous for electron transfer on the catalyst surface, inhibiting photogenerated carrier recombination, unveiling active sites, and enhancing the photocatalytic activity. Huang and Nie synthesized $TiO_2$/BiOI composite catalysts with nanoflower-like and heterogeneous structures using the solvothermal method. These composite catalysts outperform single-component BiOI catalysts in various metrics, including lower rates of photogenerated electron−hole recombination, larger specific surface areas, and superior photocatalytic efficiency.[24] In Figure 4e,f, BiOI microspheres, ranging from


https://doi.org/10.1021/acsomega.3c05569
ACS Omega 2024, 9, 361−370

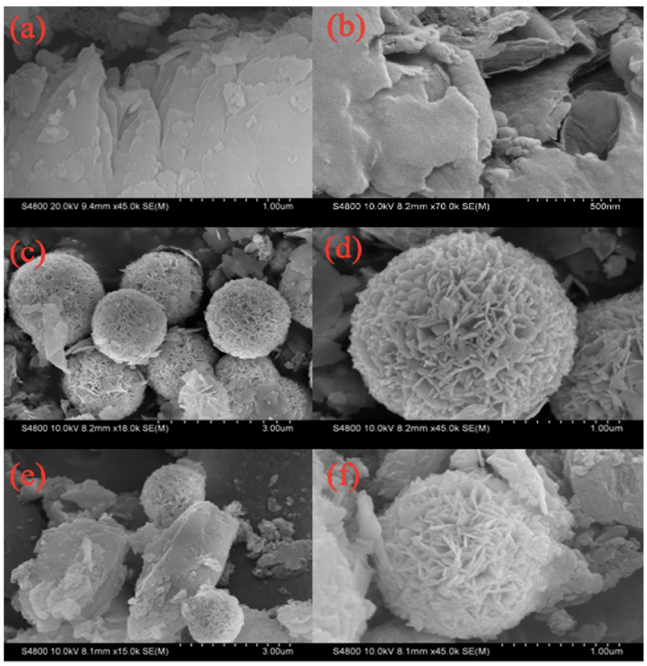


**Figure 4.** SEM images of g-$C_3N_4$ (a/b), BiOI (c/d), and g-$C_3N_4$/BiOI (e/f).

400 to 500 nm in diameter, are seen adhering to the surface of g-$C_3N_4$, signifying a strong interaction between the two materials. Furthermore, zeta potential analysis reveals that g-$C_3N_4$ carries a negative charge of −22.4 mV, while BiOI carries a positive charge of +10.9 mV. This suggests that the heterojunction between g-$C_3N_4$ and BiOI forms through electrostatic self-assembly.[25]

As revealed by Figure 5a, the BiOI spheres within the composite materials closely adhere to the flat sheetlike structure

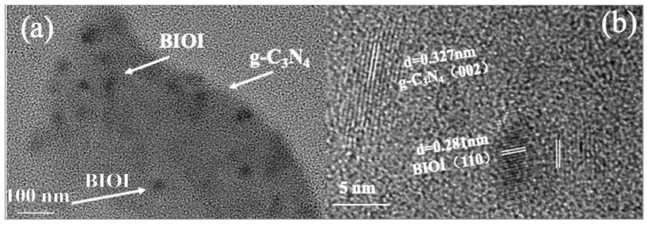


**Figure 5.** (a, b) TEM image of g-$C_3N_4$/BiOI.

of g-$C_3N_4$, corroborating the observations from SEM. In Figure 5b, the lattice stripe with a spacing of 0.327 nm is identified as corresponding to the (002) crystal plane of g-$C_3N_4$, while the lattice stripe with a 0.281 nm spacing is associated with the (110) crystal plane of BiOI. These findings lend further credence to the XRD conclusion that the g-$C_3N_4$/BiOI composite catalyst has been successfully synthesized. Moreover, the intermingling of BiOI spheres and g-$C_3N_4$ sheets points to the formation of a heterojunction between the two materials. This composite showcases g-$C_3N_4$'s unique sheet structure, which enhances the separation and transfer of photocarriers, subsequently boosting its catalytic performance.[26]

The photocatalytic activity of g-$C_3N_4$, BiOI, and their composite g-$C_3N_4$/BiOI was assessed through UV−vis DRS, focusing on changes in the optical absorption and indirect energy band gaps. As illustrated in Figure 6a, the absorption edge for the g-$C_3N_4$/BiOI composite was red-shifted to 485 nm, compared to the 450 nm observed for pure g-$C_3N_4$. This shift indicates that when combined with BiOI—which has an absorption edge at 670 nm—g-$C_3N_4$ and BiOI form a heterojunction structure characterized by well-matched energy levels. This unique structure augments the composite's ability to absorb visible light, thereby enhancing light utilization and facilitating redox reactions within the composite material. As illustrated in Figure 6b, the calculated band gap values ($E_g$) for g-$C_3N_4$ and BiOI are +2.73 and +1.85 eV, respectively, based on the plot correlating $(\alpha h\upsilon)^2$and $h\upsilon$. Concurrently, the valence band energy ($E_{VB}$) for BiOI and g-$C_3N_4$ was determined to be +2.62 and +1.61 eV, respectively, while the conduction band energy ($E_{CB}$) was found to be +0.77 eV for BiOI and −1.12 eV for g-$C_3N_4$, according to the relevant equations.[27]

$$E_{VB} = \chi - E^e + 0.5E_g \quad (1)$$

$$E_{CB} = E_{VB} - E_g \quad (2)$$

$\chi$ represents the absolute electronegativity of the semiconductor, $E_g$ denotes the bandgap value of the semiconductor, and $E^e$ is the free electron energy on the scale of the hydrogen atom, equal to 4.5 eV.

Analyzed by Mott−Schottky plots, the BiOI curves show negative slopes and the g-$C_3N_4$ curves show positive slopes, which are consistent with the characteristics of p- and n-type semiconductors, respectively.[28,29] The composite catalyst g-$C_3N_4$/BiOI exhibits an inverted "V-shape", indicating the formation of a p−n heterojunction.[30] The conduction and valence bands of g-$C_3N_4$ are positioned higher than those of BiOI, and this difference facilitates the transfer of photogenerated electrons from the n-type g-$C_3N_4$ semiconductor to the p-type BiOI semiconductor. Concurrently, photogenerated holes move from BiOI to g-$C_3N_4$. These simultaneous transfers result in the creation of an internal electric field and the generation of coupling forces. Moreover, the strong interactions between the constituent materials contribute to the formation of a tightly coupled p−n heterojunction, thereby accelerating charge transfer.[31]

Figure 7 illustrates the characteristic emission peaks for both g-$C_3N_4$/BiOI and g-$C_3N_4$. Notably, the PL spectra of g-$C_3N_4$/BiOI exhibit a blue shift of approximately 10 nm, which is attributed to the robust intermolecular bonding between g-$C_3N_4$ and BiOI.[32] Concurrently, the emission peak intensity for g-$C_3N_4$/BiOI is markedly lower than that of pure g-$C_3N_4$. This reduction in intensity arises from the suppression of electron−hole recombination, facilitated by the complexation of g-$C_3N_4$ with BiOI. This interaction enhances the separation of induced charge carriers, thereby diminishing fluorescence intensity, accelerating photogenerated charge separation,[33] and amplifying the photocatalyst's degradation capabilities.

To explore the alterations in the surface characteristics of g-$C_3N_4$/BiOI composites following the incorporation of g-$C_3N_4$, we examined $N_2$ adsorption−desorption curves and pore diameter distributions, as depicted in Figure 8. The pore attributes are detailed in Table 1. The graphs reveal that both samples exhibit low adsorption levels in the low-pressure region; however, the quantity of adsorbed gas escalates as the component partial pressures increase. The specific surface areas for g-$C_3N_4$ and g-$C_3N_4$/BiOI are 26.79 and 32.66 $m^2/g$, respectively. Notably, the specific surface area of the g-$C_3N_4$/BiOI composite shows a marginal increase compared to that of pure g-$C_3N_4$. This modest enhancement is potentially


https://doi.org/10.1021/acsomega.3c05569
ACS Omega 2024, 9, 361−370

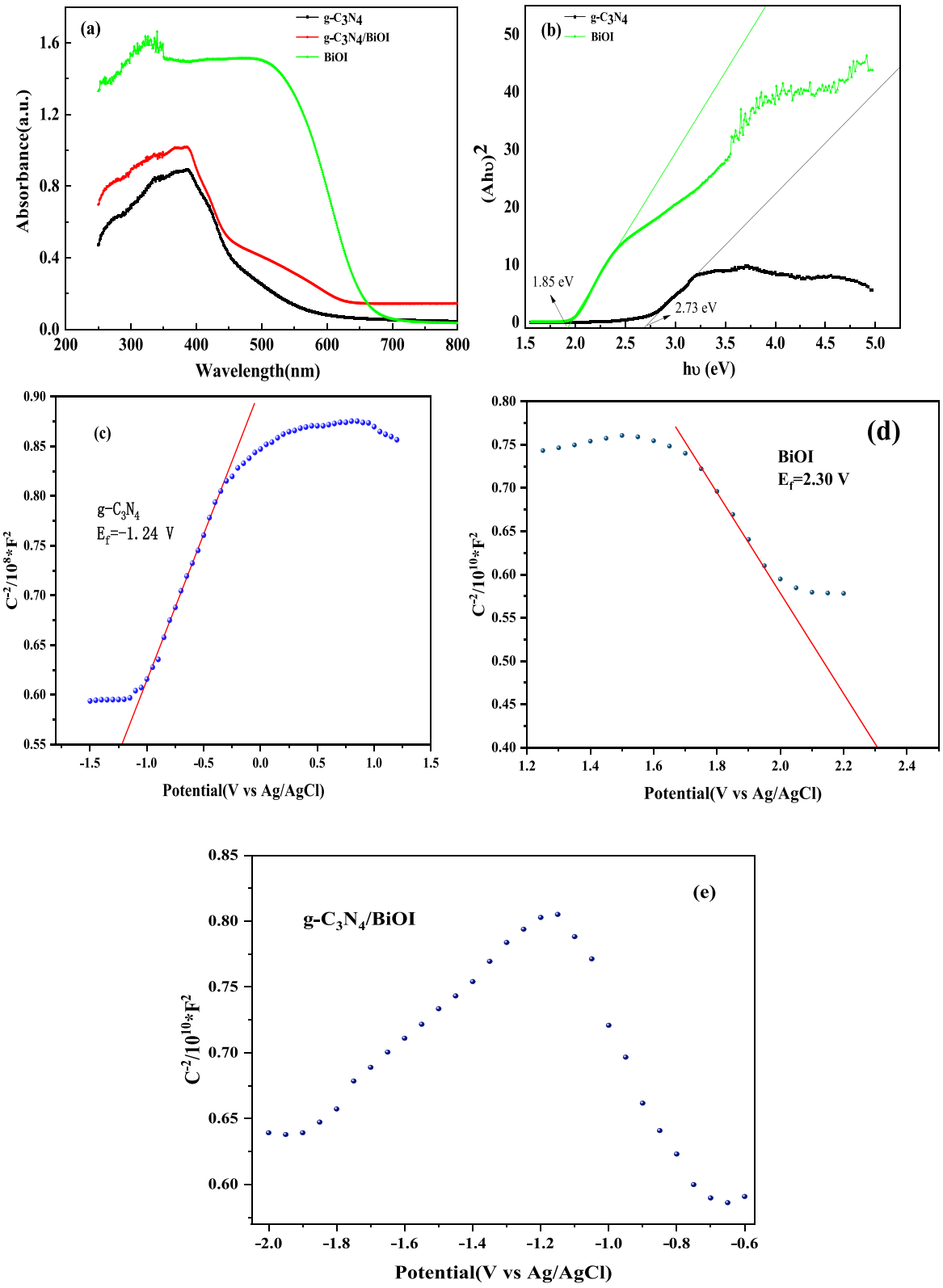


**Figure 6.** (a) UV−vis DRS spectra of BiOI, g-$C_3N_4$, and g-$C_3N_4$/BiOI. (b) Estimated band gap of g-$C_3N_4$ and g-$C_3N_4$/BiOI. (c−e) Mott−Schottky plots of g-$C_3N_4$, BiOI, and g-$C_3N_4$ /BiOI.

attributable to the addition of BiOI particles, which partially coat the g-$C_3N_4$ surface without causing a significant increase.

The photocatalytic efficacy of g-$C_3N_4$/BiOI composites, compared to pure g-$C_3N_4$, was systematically examined through AR solution degradation tests under illuminated conditions. Control experiments were also conducted using AR solutions in photocatalyst-free light and in dark environments with composite photocatalysts. The g-$C_3N_4$/BiOI composite outperformed pure g-$C_3N_4$, which had a degradation rate of 50.15%. Specifically, g-$C_3N_4$/BiOI-15% composites achieved a 74.64%



https://doi.org/10.1021/acsomega.3c05569
ACS Omega 2024, 9, 361−370

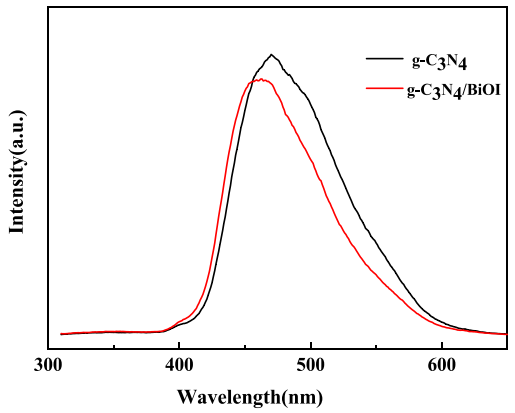


**Figure 7.** PL spectra of g-$C_3N_4$ and g-$C_3$N4/BiOI.

degradation of AR within 150 min of light exposure, while the dark condition degradation rate was 18.21%.

The photocatalytic performance was found to improve incrementally with the addition of up to 15 mg of BiOI. This enhancement is attributed to the efficient charge separation and transfer between the BiOI spheres and g-$C_3N_4$ nanosheets. However, the performance slightly declined with further increases in BiOI content. This decline is likely due to BiOI's narrow band gap, which serves as a charge carrier recombination center, thereby facilitating electron−hole pair recombination. Additionally, a higher BiOI content results in increased competition for light absorption between g-$C_3N_4$ and BiOI, which in turn delays the migration of electron−hole pairs.

According to the Langmuir−Hinshelwood kinetic model, the degradation process of the AR solution can be described by a specific kinetic equation.

The rate constants $k$ for the g-$C_3N_4$/BiOI composite photocatalysts and their pure g-$C_3N_4$ counterparts were computed based on the data in Figure 9b and are displayed in Figure 9c. Specifically, the rate constants $k$ for g-$C_3N_4$/BiOI and pure g-$C_3N_4$ photocatalysts, across various BiOI composite ratios, were measured as 0.0038, 0.0062, 0.0074, 0.0078, 0.0072, 0.0071, and 0.0067 $min^{-1}$, respectively. These findings clearly demonstrate that the g-$C_3N_4$/BiOI-15% composite exhibits a superior denitrification rate for AR compared with other photocatalysts, thereby reinforcing the outcomes of the preceding photocatalytic performance analysis.

The g-$C_3N_4$/BiOI composite catalysts exhibited excellent photocatalytic degradation ability, which was mainly attributed to the presence of a large number of active species with strong redox properties throughout the reaction process, among which

**Table 1. Surface Features of g-$C_3N_4$ and g-$C_3N_4$/BiOI**

| sample | specific surface area/($m^2$/g) | pore volume ($cm^3$/g) | average aperture (nm) |
|---|---|---|---|
| g-$C_3N_4$ | 26.79 | 0.147 | 21.96 |
| g-$C_3N_4$/BiOI | 32.66 | 0.149 | 18.26 |

$-O_2^-$, $^{\cdot}OH^-$, and $h^+$ were the main active substances for the conventional aqueous-phase photocatalytic degradation of pollutants. To pinpoint the principal active agents in the photocatalytic degradation of AR, we conducted radical scavenging assays using disodium EDTA ($Na_2EDTA$) for $h^+$, benzoquinone (BQ) for $O_2^-$, and isopropanol (IPA) for $^{\cdot}OH^-$. Figure 10 reveals that adding a 1.0 mmol/L scavenger to the reaction mixture substantially reduced the AR degradation rate. Specifically, under visible light irradiation for 150 min, the photodegradation of AR dropped to 62.71, 50.40, and 22.44% when $Na_2EDTA$, IPA, and BQ were present, respectively, which indicated that $h^+$, $-OH^-$, and $-O_2^-$ were the major reactive species in the reaction system.[34] Notably, the inclusion of BQ exerted a profound impact on the photocatalytic oxidation of AR, underscoring that photogenerated $^{\cdot}O_2^-$ plays a pivotal role, with −OH playing a secondary role in AR's photodegradation when using the g-$C_3N_4$/BiOI composite catalyst under visible light conditions.

Moreover, the $E_{VB}$ of g-$C_3N_4$, at +1.61 eV, is lower than the reduction energies for both OH/$^{\cdot}$OH (+2.38 eV) and $H_2O$/$^{\cdot}$OH (+2.72 eV). In contrast, the $E_{VB}$ value for BiOI, at +2.62 eV, exceeds the activation energy for OH/$^{\cdot}$OH (+2.38 eV), and BiOI oxidizes $H_2O$ to produce $^{\cdot}OH$. Additionally, the conduction band energy ($E_{CB}$) of g-$C_3N_4$ surpasses that of $O_2$/$^{\cdot}O_2^-$ (−0.33 eV), and the electrons in g-$C_3N_4$ easily react with adsorbed oxygen to reduce $O_2$ to form the highly oxidizing radical $^{\cdot}O_2$-. This is in line with the results from radical scavenging experiments and suggests that photogenerated $^{\cdot}O_2^-$ possesses enhanced oxidative capabilities, enabling more efficient degradation of AR. It can also directly interact with dye molecules to yield the end product. Based on these observations, we have proposed a mechanism for the photodegradation of AR over the g-$C_3N_4$/BiOI composite under visible light, as illustrated in Figure 11.

## 4. CONCLUSIONS

In this study, we synthesized g-$C_3N_4$/BiOI nanomicrosphere composite catalysts using heat polycondensation, hydrothermal, and hybrid techniques. These composite catalysts demonstrated superior performance in the photocatalytic degradation of AR. The enhanced catalytic efficiency is attributed to the optimized

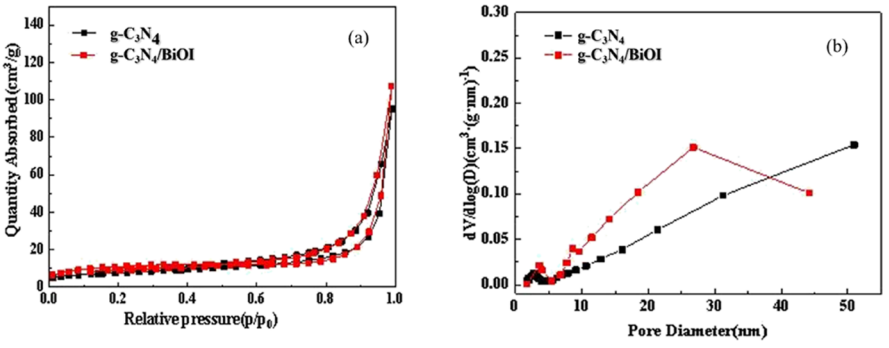


**Figure 8.** (a) $N_2$ adsorption−desorption isotherm of g-$C_3N_4$ and g-$C_3N_4$/BiOI. (b) Pore diameter distributions of g-$C_3N_4$ and g-$C_3N_4$/BiOI.


https://doi.org/10.1021/acsomega.3c05569
ACS Omega 2024, 9, 361−370

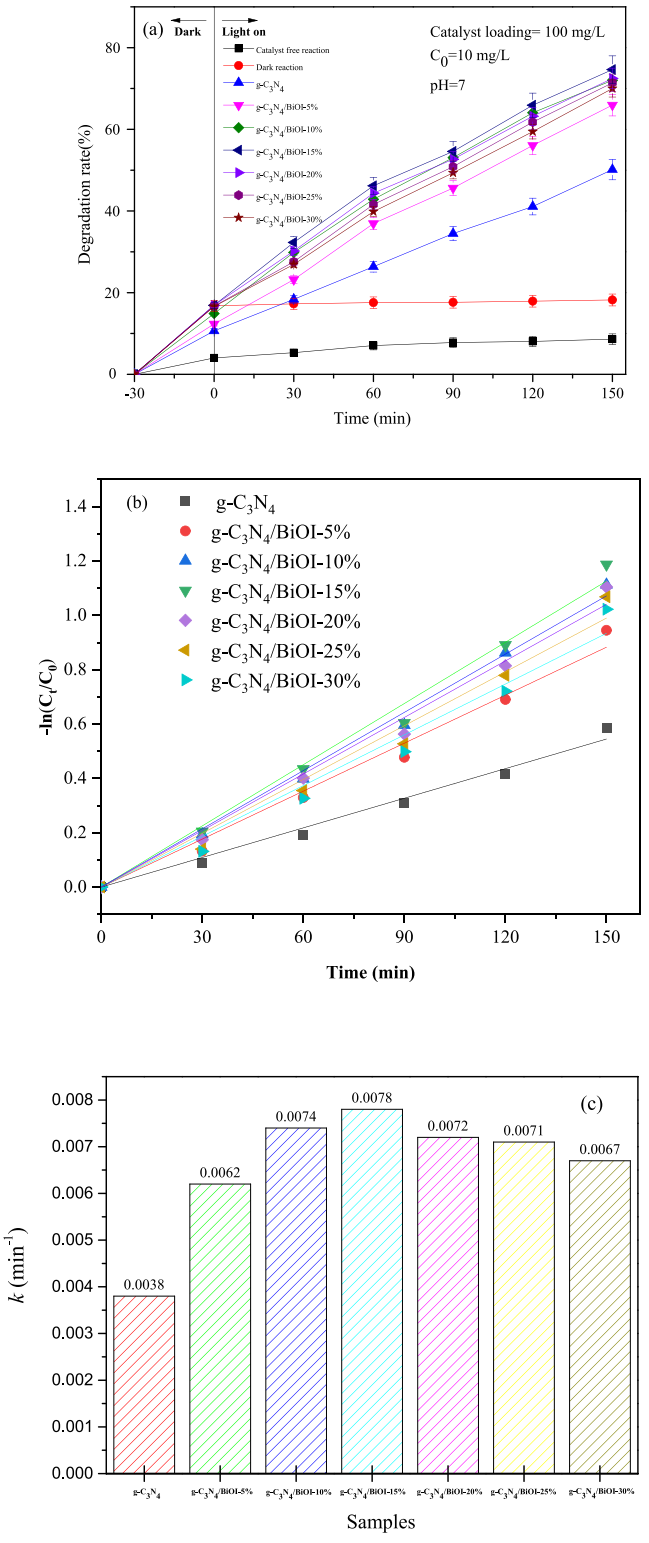


**Figure 9.** (a) Photocatalytic activity test. (b) Kinetic linear fitting results of AR degradation of each sample. (c) Photocatalytic degradation kinetic parameters.

photoelectron transfer facilitated by the p−n heterojunction formed between the g-$C_3N_4$ and BiOI components. While numerous studies have explored the degradation of organic dyes using g-$C_3N_4$/BiOI composites, there is a notable gap in the literature concerning their application to amaranth dye degradation. Consequently, further investigation into the photocatalytic capabilities of g-$C_3N_4$/BiOI composites for amaranth dye degradation holds practical implications for industrial wastewater treatment, particularly for food dye waste.

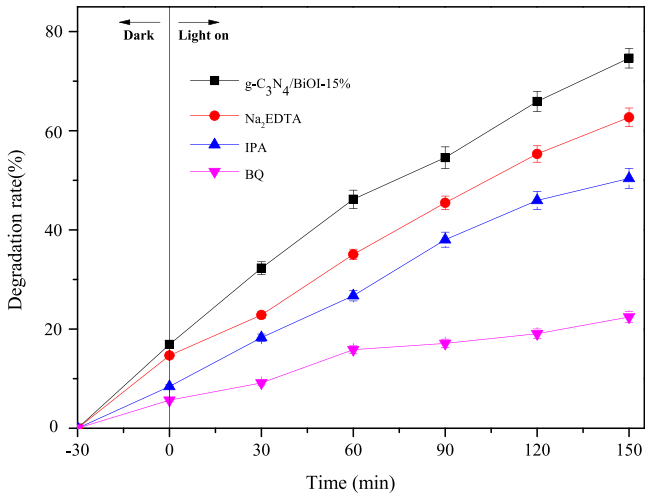


**Figure 10.** Effect of the scavengers on the degradation rate of solution.

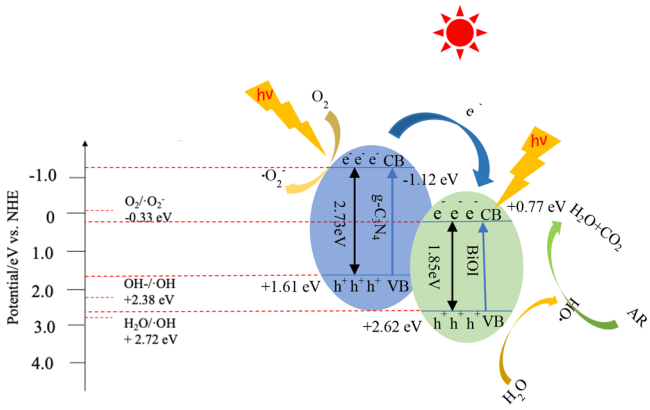


**Figure 11.** Photocatalytic mechanism diagram.

## AUTHOR INFORMATION


### Corresponding Author

**Zhi Xia** − *School of Food Science and Engineering, Harbin University of Commerce, Harbin 150028, China;* orcid.org/0000-0001-8736-2028; Email: guan_li111@163.com

### Authors

**Junsheng Li** − *School of Food Science and Engineering, Harbin University of Commerce, Harbin 150028, China*

**Li Guan** − *School of Food Science and Engineering, Harbin University of Commerce, Harbin 150028, China*

**Liming Jiang** − *School of Food Science and Engineering, Harbin University of Commerce, Harbin 150028, China*

**Meiyan Xu** − *School of Food Science and Engineering, Harbin University of Commerce, Harbin 150028, China*

**Jiahui Li** − *School of Food Science and Engineering, Harbin University of Commerce, Harbin 150028, China*

**Jinlong Zuo** − *School of Food Science and Engineering, Harbin University of Commerce, Harbin 150028, China*

**Chong Tan** − *School of Food Science and Engineering, Harbin University of Commerce, Harbin 150028, China*

Complete contact information is available at:




https://doi.org/10.1021/acsomega.3c05569
ACS Omega 2024, 9, 361−370

https://pubs.acs.org/10.1021/acsomega.3c05569

### Notes

The authors declare no competing financial interest.

## ■ ACKNOWLEDGMENTS

This research was funded by Heilongjiang Provincial Natural Science Foundation Joint Steering Project, grant number LH2022E090. J.L. developed comprehensive experimental concepts; L.G. executed tests and finalized the manuscript, including significant translation work. L.J. and M.X. spearheaded the study, while J.L. managed data organization and graphical representation. J.Z. performed a thorough review of the completed manuscript. C.T. supplied financial backing for the research and oversaw the entire experimental process. Z.X. contributed by reviewing the final manuscript and facilitating correspondence. There is no potential conflict of interest in this paper.

## ■ REFERENCES

(1) Jindal, H.; Kumar, D.; Sillanpaa, M.; Nemiwal, M. Current progress in polymeric graphitic carbon nitride-based photocatalysts for dye degradation. *Inorg. Chem. Commun.* **2021**, *131*, No. 108786.

(2) Dai, K.; Lu, L.; Liang, C.; Liu, Qi; Zhu, G. Heterojunction of facet coupled g-$C_3N_4$/surface-fluorinated $TiO_2$ nanosheets for organic pollutants degradation under visible LED light irradiation. *Appl. Catal. B Environ.* **2014**, *156*, 331−340.

(3) Guo, X.; Li, X.; Qin, L.; Kang, S.; Li, G. A highly active nano-micro hybrid derived from Cu-bridged $TiO_2$/porphyrin for enhanced photocatalytic hydrogen production. *Appl. Catal. B Environ.* **2019**, *243*, 1−9.

(4) Wang, S.; Li, D.; Sun, C.; Yang, S.; Guan, Y.; He, H. Synthesis and characterization of g-$C_3N_4$/$Ag_3VO_4$ composites with significantly enhanced visible-light photocatalytic activity for triphenylmethane dye degradation. *Appl. Catal. B Environ.* **2014**, *144*, 885−892.

(5) Cui, Y.; Wang, Y.; Wang, H.; Cao, F.; Chen, F. Polycondensation of ammonium thiocyanate into novel porous g-$C_3N_4$ nanosheets as photocatalysts for enhanced hydrogen evolution under visible light irradiation. *Chinese. J. Catal.* **2016**, *37*, 1899−1906.

(6) Jiang, X.; Qiao, K.; Feng, Y.; Sun, L.; Jiang, N.; Wang, J. Self-assembled synthesis of porous sulfur-doped g-$C_3N_4$ nanotubes with efficient photocatalytic degradation activity for tetracycline. *J. Photoch. Photobio. A* **2022**, *433*, No. 114194.

(7) Bandyopadhyay, A.; Ghosh, D.; Kaley, N.; Pati, S. Photocatalytic Activity of g-$C_3N_4$ Quantum Dots in Visible Light: Effect of Physicochemical Modifications. *Phys. Chem.* **2017**, *121*, 1982−1989.

(8) He, Y.; Cai, J.; Li, T.; Wu, Y.; Lin, H.; Zhang, L.; Luo, M. Efficient degradation of RhB over $GdVO_4$/g-$C_3N_4$ composites under visible-light irradiation. *Chem. Eng. J.* **2013**, *215*, 721−730.

(9) Li, M.; Wu, Y.; An, S.; Yan, Z. Au NP-Decorated g-$C_3N_4$-Based Photoelectochemical Biosensor for Sensitive Mercury Ions Analysis. *ACS omega.* **2022**, *7* (23), 19622−19630.

(10) Sattari, M.; Farhadian, M.; Nazar, A.; Moghadam, M. $NiFe_2O_4$/g-$C_3N_4$ heterostructure with an enhanced ability for photocatalytic degradation of tetracycline hydrochloride and antibacterial performance. *J. Photochem. Photobiol. A* **2022**, *431*, 114065.

(11) Liu, S.; Zada, A.; Yu, X.; Liu, F.; Jin, G. $NiFe_2O_4$/g-$C_3N_4$ heterostructure with an enhanced ability for photocatalytic degradation of tetracycline hydrochloride and antibacterial performance. *Chemosphere.* **2022**, *307*, No. 135717.

(12) Li, H.; Wang, D.; Miao, C.; Xia, F.; Wang, Y.; Liu, C.; Che, G. g-$C_3N_4$/BiOI S-scheme heterojunction: A 2D/2D model platform for visible-light-driven photocatalytic $CO_2$ reduction and pollutant degradation. *J. Environ. Chem. Eng.* **2022**, *10* (4), No. 108201.

(13) Changlu Shao*Orcid, Shu Yang, Xiaowei Li, Xiaohui Guo, Xiaoxiao Wang, Xinghua Li*, and Yichun Liu Zhou, X.; Shao, C.; Yang, S.; Li, X.; Guo, X.; Wang, X.; Li, X.; Liu, Y. Heterojunction of g-$C_3N_4$/BiOI immobilized on flexible electrospun polyacrylonitrile nanofibers: facile preparation and enhanced visible photocatalytic activity for floating photocatalysis. *ACS Sustainable Chem. Eng.* **2018**, *6*, 2316−2323.

(14) Qiu, P.; Yao, J.; Chen, H.; Jiang, F.; Xie, X. Enhanced visible-light photocatalytic decomposition of 2,4-dichlorophenoxyacetic acid over $ZnIn_2S_4$/g-$C_3N_4$ photocatalyst. *Hazard. Mater.* **2016**, *317*, 158−168.

(15) Liu, R.; Tan, C.; Li, J.; Zuo, J. Rational design of a novel C/ZnO/BiOI composite for efficient visible-light-driven photocatalysis. *Mater. Lett.* **2021**, *304*, No. 130564.

(16) Aghdam, S.; Haghighi, M.; Allahyari, S.; Yosefi, L. Precipitation dispersion of various ratios of BiOI/BiOCl nanocomposite over g-$C_3N_4$ for promoted visible light nanophotocatalyst used in removal of acid orange 7 from water. *J. Photoch. Photobio. A* **2017**, *338*, 201−212.

(17) Wang, Q.; Li, Y.; Huang, L.; Zhang, F.; Wang, H.; Wang, C.; Zhang, Y.; Xie, M.; Li, H. Enhanced photocatalytic degradation and antibacterial performance by GO/CN/BiOI composites under LED light. *Appl. Surf. Sci.* **2019**, *497*, No. 143753.

(18) Dou, K.; Peng, C.; Wang, R.; Cao, H.; Yao, C.; Qiu, J.; Liu, J.; Tsidaeva, N.; Wang, W. S-scheme tubular g-$C_3N_4$/BiOI heterojunctions for boosting photodegradation of tetracycline and Cr (VI): Mechanism insight, degradation pathway and DFT calculation. *Chem. Eng. J.* **2023**, *455*, No. 140813.

(19) Tian, N.; Huang, H.; Wang, S.; Zhang, T.; Du, X.; Zhang, Y. Facet-charge-induced coupling dependent interfacial photocharge separation: A case of BiOI/g-$C_3N_4$ p−n junction. *Appl. Catal. B. Environ* **2020**, *267*, No. 118697.

(20) Li, Z.; Chen, Q.; Lin, Q.; Chen, Y.; Liao, X.; Yu, H.; Yu, C. Three-dimensional P-doped porous g-$C_3N_4$ nanosheets as an efficient metal-free photocatalyst for visible-light photocatalytic degradation of Rhodamine B model pollutant. *J. Taiwan. Inst. Chem. E* **2020**, *114*, 249−262.

(21) Li, K.; Jiang, Y.; Rao, W.; Li, Y.; Liu, X.; Zhang, J.; Xu, X.; Li, K. Cooperative coupling strategy for constructing 0D/2D carbon nitride composites with strengthened chemical interaction for enhanced photocatalytic applications. *Chem. Eng. J.* **2022**, *431*, No. 134075.

(22) Shi, L.; Liang, L.; Ma, J.; Meng, Y.; Zhong, S.; Wang, F.; Sun, J. Highly efficient visible light-driven Ag/AgBr/ZnO composite photocatalyst for degrading Rhodamine B. *Ceram. Int.* **2014**, *40*, 3495−3502.

(23) Jiang, T.; Jin, J.; Hou, J.; Tahir, M.; Idress, F. $Bi_4O_5I_2$/nitrogen-doped hierarchical carbon (NHC) composites with tremella-like structure for high photocatalytic performance. *Chemosphere* **2019**, *22*, 426−433.

(24) Huang, Q.; Nie, E. Preparation of $TiO_2$/BiOI and its visible photocatalytic properties. *Micro. Tech.* **2022**, *59*, 1090−1097.

(25) Li, S.; Wang, T.; Zhang, H.; Chang, L.; Ye, J. Electrostatic self-assembly of nanosized carbon nitride nanosheet onto a zirconium metal−organic framework for enhanced photocatalytic $CO_2$ reduction. *Adv. Funct. Mater.* **2015**, *25*, 5360−5367.

(26) Zhang, C.; Fei, W.; Wang, H.; Li, N.; Chen, D.; Xu, Q.; Li, H.; He, J.; Lu, J. pn Heterojunction of BiOI/ZnO nanorod arrays for piezo-photocatalytic degradation of bisphenol A in water. *Hazard Mater.* **2020**, *399*, No. 123109.

(27) Li, Y.; Wang, Q.; Huang, L.; Xu, X.; Xie, M.; Wang, H.; Huang, S.; Zhang, F.; Zhao, Z.; Yang, J. Enhanced LED-light-driven photocatalytic antibacterial by g-$C_3N_4$/BiOI composites. *Sci. Mater.* **2019**, *30*, 2783−2794.

(28) Tan, H.; Zhou, P.; Liu, M.; Zhang, Q.; Liu, F.; Guo, H.; Zhou, Y.; Chen, Y.; Zeng, L.; Gu, L.; Zheng, Z.; Tong, M.; Guo, S. Photocatalysis of water into hydrogen peroxide over an atomic Ga-$N_5$ site. *Nature Synthesis* **2023**, *2* (6), 557−563.

(29) Yan, M.; Hua, Y.; Zhu, F.; Gu, W.; Jiang, J.; Shen, H.; Shi, W. Fabrication of nitrogen doped graphene quantum dots-BiOI/$MnNb_2O_6$ pn junction photocatalysts with enhanced visible light efficiency in photocatalytic degradation of antibiotics. *Applied Catalysis B: Environmental* **2017**, *202*, 518−527.

(30) Wen, X.; Niu, C.; Zhan, L.; Zeng, G. Fabrication of $SnO_2$ nanopaticles/BiOI n−p heterostructure for wider spectrum visible-light

photocatalytic degradation of antibiotic oxytetracycline hydrochloride. *ACS Sustainable Chem. Eng.* **2017**, *5*, 5134−5147.
(31) Luo, J.; Zhou, X.; Ma, L.; Xu, X. Enhanced visible-light-driven photocatalytic activity of $WO_3$/BiOI heterojunction photocatalysts. *Mol. Catal. Chem.* **2015**, *410*, 168−176.
(32) Piao, H.; Choi, G.; Jin, X.; Hwang, S.; Song, Y.; Cho, S.; Choy, J. Monolayer graphitic carbon nitride as metal-free catalyst with enhanced performance in photo-and electro-catalysis. *Nano-Micro Lett.* **2022**, *14*, 55.
(33) Ye, L.; Su, Y.; Jin, X.; Xie, H.; Zhang, C. Recent advances in BiOX (X= Cl, Br and I) photocatalysts: synthesis, modification, facet effects and mechanisms. *Sci. Nano.* **2014**, *1*, 90−112.
(34) Li, J.; Guan, R.; Zhang, J.; Zhao, J.; Zhai, H.; Sun, D.; Qi, Y. Preparation and photocatalytic performance of dumbbell $Ag_2CO_3$−ZnO heterojunctions. *ACS omega* **2020**, *5* (1), 570−577.


https://doi.org/10.1021/acsomega.3c05569
*ACS Omega* 2024, 9, 361−370